Critical charges for droplet collisions

A. Dubey [1], G. P. Bewley,[2] K. Gustavsson,[1] and B. Mehlig [1]
[1]*Department of Physics, Gothenburg University, 41296 Gothenburg, Sweden*
[2]*Sibley School of Mechanical and Aerospace Engineering, Cornell University, Ithaca, New York 14853, USA*

(Received 12 September 2022; accepted 3 May 2024; published 19 July 2024)

Two micron-sized water droplets approaching each other do not always coalesce due to the cushioning effect of the air between them. When the droplets do not carry any electrical charges, one needs to consider the breakdown of hydrodynamics at very small scales to decide whether the droplets collide and coalesce or not. In contrast, two approaching droplets that are oppositely charged always coalesce if the charges are large enough. To find the charge for which the transition to charge-dominated collisions occurs, we computed the collision efficiency of charged, hydrodynamically interacting droplets settling in quiescent air, including the noncontinuum regime at small interfacial distances. For oppositely charged droplets, we find that the transition occurs when a saddle point of the relative droplet dynamics exits the region within which the continuum hydrodynamics breaks down. For cloud droplets with radii 16 and 20 μm, we observe that the transition occurs at $\sim 10^3$ elementary charges e. For charges smaller than this, we predict that the coalescence rate depends primarily upon the Knudsen number (Kn, the ratio of the mean-free-path of air to the mean droplet radius), whereas coalescence for much larger charges does not depend upon Kn. For droplets charged with the same polarity, we find the critical charge to be substantially larger ($\sim 10^4\, e$ for the above radii) for reasons that we discuss.

DOI: 10.1103/PhysRevFluids.9.074302

I. INTRODUCTION

How do micron-sized cloud droplets grow large enough to make drizzle or rain? The question relates to the fundamental mechanisms that determine droplet-size distributions in atmospheric clouds [1–3]. In clouds of droplets with different sizes, collisions occur due to differential settling: the broader the droplet size distribution, the more rapid the droplet growth [4,5]. This process needs, however, to be initiated, and the way size differences develop initially is an open question. Saffman and Turner [6] describe theoretically how atmospheric turbulence causes droplets of similar size to collide, but for typical droplets this process is too slow to explain observations. On the other hand, if droplet collisions are independent from one another and random, then their collision times are Poisson distributed, and fluctuations can cause a small number of droplets to grow relatively rapidly [7].

Hydrodynamic interactions between approaching droplets reduce the likelihood that they collide [8], which complicates the prediction of collision rates. The effect can be described by the collision efficiency, or the ratio of the collision cross section of hydrodynamically interacting droplets to the cross section for droplets that do not interact, the latter being proportional to $(a_1 + a_2)^2$ for neutral droplets with radii a_1 and a_2. Theoretically, the hydrodynamic interaction force diverges at very small distances, which prevents the neutral droplets approaching in a quiescent fluid from

colliding at all [9]. Cloud droplets do collide, however, and the contradiction with the theory is partly resolved by considering the way in which continuum hydrodynamics breaks down at droplet separations of the order of the mean-free path of air [10]. The consequences of noncontinuum effects include a weakening of the interaction force between the droplets, and a resulting collision efficiency that depends on the Knudsen number (Kn), which is equal to the mean-free path divided by the mean droplet radius. For a shear flow, the particular dependence of the collision rate on Kn and on the nondimensional relative settling speeds of the droplets can be understood in terms of an intricate sequence of bifurcations of the collision dynamics [11].

Hydrodynamic interactions, even when considering the breakdown of continuum hydrodynamics, result in a significant *reduction* of the Saffman-Turner collision rate [12], which is already too slow to explain observations. Therefore, additional factors are thought to play a role in determining the collision dynamics of settling droplets. For instance, the inertia of water droplets allows them to detach from the surrounding turbulent airflow, leading to larger collision rates [13–15]. Recent work shows that inertia can also reduce collision rates by promoting bouncing [16]. To simplify the analysis, the inertial effect is often neglected [e.g., 11,12,17]. Klett and Davis [18] show how the collision rate of similar-sized droplets depends sensitively on the droplet Reynolds number, which is a measure of the effect of convective fluid inertia upon the disturbance flow caused by the settling droplets. The reason for this effect is that the Stokes problem for the collision dynamics is degenerate: equal-sized droplets neither approach nor separate, and convective fluid inertia breaks this degeneracy [19]. Furthermore, droplets approaching contact may deform each other if the hydrodynamic forces on the droplets become comparable with the surface tension of the droplets [20]. The collision dynamics for nonspherical droplets is more complicated than for spherical ones. Finally, the short-range van der Waals forces can increase collision rates at small Knudsen numbers [21].

Small water droplets in thunderclouds and in warm rain clouds carry electrical charges [22,23]. These electrical charges can affect the dynamics of water droplets and the rate at which they collide [1]. In addition to direct electrical interactions between droplets, the electrical charges make the droplet dynamics sensitive to external electric fields that could lead to enhanced collision rates [24,25]. The dielectric nature of water droplets may further affect the dynamics. For instance, the coupling between the hydrodynamic and electrical forces for dielectric droplets in a dielectric medium leads to charge-driven droplet deformation [26]. Furthermore, the finite electrical conductivity of droplets can lead to a phenomenon such a tip streaming, absent for perfect conductors [27].

How much charge is required to make a significant difference to the collision dynamics, and when do we need to incorporate charge in our predictions of droplet collision rates? This question has a long history, but it has not yet been answered. For instance, Davis [28] finds for droplet radii of about 20 μm, the typical size of cloud droplets, that more than 800 elementary charges e are required for the Coulomb force to affect the collision efficiency, while Tinsley and Zhou [29] suggest that it may take at least 10^4 e. These differences are not surprising given that the estimates are based on idealized models that either do not account for the way that hydrodynamic forces change as droplets approach each other [29–32], or do not consider how the hydrodynamic approximation breaks down for separations smaller than the mean-free path [28–32]. Indeed, Abbott [33] finds that the predictions fail to explain experimental observations.

Magnusson *et al.* [34] uses models for hydrodynamic and electrical interactions valid at large droplet separations to analyze the collision efficiency of strongly and oppositely charged 20-μm droplets settling in quiescent air. The collision efficiency is determined by a stable manifold of a high-dimensional saddle point of the relative droplet dynamics. At the saddle point, the larger droplet travels below the smaller one, so that Coulomb attraction, hydrodynamic interactions, and the difference of the gravity forces cancel, resulting in a steady state. When the charges are strong enough, droplets at the saddle point are far enough apart that noncontinuum effects do not matter, and that hydrodynamic interactions can be modeled by their large-distance asymptotes. To find the transition between the large-charge regime considered in Magnusson *et al.* [34], and the small-charge regime considered in the prior work discussed above, we need better models.

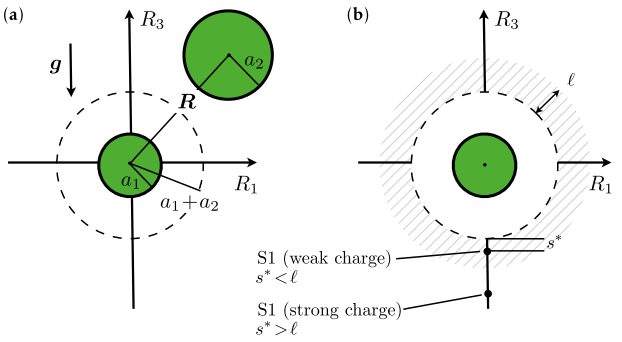

FIG. 1. (a) Shows a schematic of two droplets with radii $a_1 < a_2$ settling in a quiescent fluid. The separation vector between their centers-of-mass is $\boldsymbol{R}$. Also shown is the collision sphere around the smaller droplet (dashed). The droplets collide if the center-of-mass of the larger one hits the collision sphere. Gravity points in the negative R_3 direction. (b) Illustrates two regimes of the collision dynamics, distinguished by the location of the fixed point S1 (see text). For charges weaker than the critical charge, S1 is inside the region where hydrodynamics breaks down (hashed area), at distance $s^* \equiv R^* - 2\overline{a} < \ell$. For charges stronger than the critical charge, the fixed point lies outside, $s^* > \ell$.

To explore the physics of droplets with intermediate charges, we performed numerical simulations of droplet collision dynamics that take into account all the necessary physics, such as droplet inertia and hydrodynamic interaction forces valid over the full range of droplet separations, including their regularization by noncontinuum effects. We modeled the droplets as perfect conductors [35], which allowed us to consider the effect of induced charges that affect the electrostatic force at small separations. This latter effect is important because induced charges can cause droplets to attract each other even when they are charged with the same polarity [36,37].

We found that a critical charge separates two qualitatively different regimes in the collision efficiency: a small-charge regime where noncontinuum effects determine collision outcomes, and a large-charge regime where electrical forces determine collision outcomes. The transition region is broad, but when charge is increased, the qualitative change occurs when a saddle point of the relative droplet dynamics exits the spatial region where noncontinuum effects dominate. We find that the critical charge depends on whether the droplets are charged with the same or with opposite polarities. For two droplets with radii 16 and 20 μm charged with the opposite polarities, the transition occurs at $\sim 10^3$ elementary charges e. When the droplets have excess charges with the same polarity, $\sim 10^4$ e are required. In addition, a bifurcation occurs around 1.5×10^4 elementary charges, which leads to two saddle points above the collision sphere. We note that droplets approaching near the symmetry, the R_3 axis in Fig. 1(a), spend considerable time in the vicinity of one of the saddle points before they diverge along its unstable manifold.

II. MODEL

A. Equations of motion

The motions of two spherical droplets $\alpha = 1, 2$ are determined by Newton's equations

$$\dot{\boldsymbol{x}}^{(\alpha)} = \boldsymbol{v}^{(\alpha)}, \tag{1a}$$

$$\dot{\boldsymbol{v}}^{(\alpha)} = \left[\boldsymbol{F}_{\mathrm{g}}^{(\alpha)} + \boldsymbol{F}_{\mathrm{h}}^{(\alpha)} + \boldsymbol{F}_{\mathrm{e}}^{(\alpha)}\right]/m_\alpha, \tag{1b}$$

$$\dot{\boldsymbol{\omega}}^{(\alpha)} = \boldsymbol{T}_{\mathrm{h}}^{(\alpha)}/I_\alpha. \tag{1c}$$

Here $\boldsymbol{x}^{(\alpha)}$ and $\boldsymbol{v}^{(\alpha)}$ are the position and velocity of droplet α, and $\boldsymbol{\omega}^{(\alpha)}$ is its angular velocity. Droplet α has mass $m_\alpha = \frac{4\pi}{3}\varrho_{\mathrm{w}} a_\alpha^3$ and moment of inertia $I_\alpha = \frac{2}{5} m_\alpha a_\alpha^2$, where a_α is the radius of droplet α,

and ϱ_w is the mass density of water. On the right-hand side of Eq. (1), $\boldsymbol{F}_g^{(\alpha)} = m_\alpha \boldsymbol{g}$ is the gravity force with gravitational acceleration $\boldsymbol{g}$, $\boldsymbol{F}_h^{(\alpha)}$ and $\boldsymbol{T}_h^{(\alpha)}$ are the hydrodynamic force and torque, and $\boldsymbol{F}_e^{(\alpha)}$ is the electrostatic force on droplet α from the other droplet. The droplets settle through quiescent air. We denote their center-of-mass separation by $\boldsymbol{R} = \boldsymbol{x}^{(2)} - \boldsymbol{x}^{(1)}$ (Fig. 1), and their relative velocity by $\boldsymbol{V} = \boldsymbol{v}^{(2)} - \boldsymbol{v}^{(1)}$.

B. Hydrodynamic forces and torques

Settling droplets disturb the air around them, leading to nonzero fluid velocity and vorticity. If the Reynolds number of the fluid flow around the droplets remains small, the flow velocity and vorticity satisfy the Stokes equations [8]. This allows to express the hydrodynamic forces $\boldsymbol{F}_h^{(\alpha)}$ and torques $\boldsymbol{T}_h^{(\alpha)}$ as linear functions of the translational and angular velocities of the droplets,

$$\begin{bmatrix} \boldsymbol{F}_h^{(1)} \\ \boldsymbol{F}_h^{(2)} \\ \boldsymbol{T}_h^{(1)} \\ \boldsymbol{T}_h^{(2)} \end{bmatrix} = \begin{bmatrix} \mathbb{A}^{(11)} & \mathbb{A}^{(12)} & \widetilde{\mathbb{B}}^{(11)} & \widetilde{\mathbb{B}}^{(12)} \\ \mathbb{A}^{(21)} & \mathbb{A}^{(22)} & \widetilde{\mathbb{B}}^{(21)} & \widetilde{\mathbb{B}}^{(22)} \\ \mathbb{B}^{(11)} & \mathbb{B}^{(12)} & \mathbb{C}^{(11)} & \mathbb{C}^{(12)} \\ \mathbb{B}^{(21)} & \mathbb{B}^{(22)} & \mathbb{C}^{(21)} & \mathbb{C}^{(22)} \end{bmatrix} \begin{bmatrix} \boldsymbol{v}^{(1)} \\ \boldsymbol{v}^{(2)} \\ \boldsymbol{\omega}^{(1)} \\ \boldsymbol{\omega}^{(2)} \end{bmatrix}. \tag{2}$$

Here $\mathbb{A}^{(\alpha\beta)}$, $\widetilde{\mathbb{B}}^{(\alpha\beta)}$, $\mathbb{B}^{(\alpha\beta)}$, and $\mathbb{C}^{(\alpha\beta)}$ are matrices with components of the form $A_{ij}^{(\alpha\beta)}$, where i, j label the spatial coordinates. These build up the grand resistance matrix that maps all velocity and angular velocity components to forces and torques. It satisfies several symmetry relations, which we briefly summarize following the discussion in Jeffrey and Onishi [38]. Due to the spherical droplet shape, the resistance matrices only depend on the droplet separation vector $\boldsymbol{R}$, and the droplet radii a_1 and a_2. By particle exchange symmetry, Eq. (2) is invariant under simultaneous relabeling $1 \leftrightarrow 2$ and transforming $\boldsymbol{R} \to -\boldsymbol{R}$. This constrains any element of the resistance tensor to obey the relation

$$\mathbb{P}^{(\alpha\beta)}(\boldsymbol{R}, a_1, a_2) = \mathbb{P}^{((3-\alpha)(3-\beta))}(-\boldsymbol{R}, a_2, a_1). \tag{3}$$

Furthermore, the reciprocal theorem, which gives relations between two different velocity and stress fields, constrains the grand resistance matrix to be symmetric [8]. This implies that the elements of the resistance matrix satisfy

$$A_{ij}^{(\alpha\beta)} = A_{ji}^{(\beta\alpha)}, \tag{4a}$$

$$\widetilde{B}_{ij}^{(\alpha\beta)} = B_{ji}^{(\beta\alpha)}, \tag{4b}$$

$$C_{ij}^{(\alpha\beta)} = C_{ji}^{(\beta\alpha)}. \tag{4c}$$

Finally, for axisymmetric particles, each tensor in the resistance matrix is axisymmetric and may be written in terms of at most two scalar functions: the radial resistance function $X_{\alpha\beta}$ and the tangential resistance function $Y_{\alpha\beta}$ [8,38]:

$$A_{ij}^{(\alpha\beta)} = -6\pi\mu \frac{a_\alpha + a_\beta}{2} \left[X_{\alpha\beta}^A \widehat{R}_i \widehat{R}_j + Y_{\alpha\beta}^A (\delta_{ij} - \widehat{R}_i \widehat{R}_j) \right], \tag{5a}$$

$$B_{ij}^{(\alpha\beta)} = -4\pi\mu \left(\frac{a_\alpha + a_\beta}{2} \right)^2 \left[Y_{\alpha\beta}^B \epsilon_{ijk} \widehat{R}_k \right], \tag{5b}$$

$$\widetilde{B}_{ij}^{(\alpha\beta)} = B_{ji}^{(\beta\alpha)}, \tag{5c}$$

$$C_{ij}^{(\alpha\beta)} = -8\pi\mu \left(\frac{a_\alpha + a_\beta}{2} \right)^3 \left[X_{\alpha\beta}^C \widehat{R}_i \widehat{R}_j + Y_{\alpha\beta}^C (\delta_{ij} - \widehat{R}_i \widehat{R}_j) \right]. \tag{5d}$$

Here μ is the dynamic viscosity of air. The Einstein summation convention is implied in Eq. 5(b) for repeated indices. The resistance functions $X_{\alpha\beta}$ and $Y_{\alpha\beta}$ are nondimensional and depend upon the radius ratio $\lambda = a_1/a_2$ and upon the nondimensional center-of-mass distance $R/\overline{a}$ between

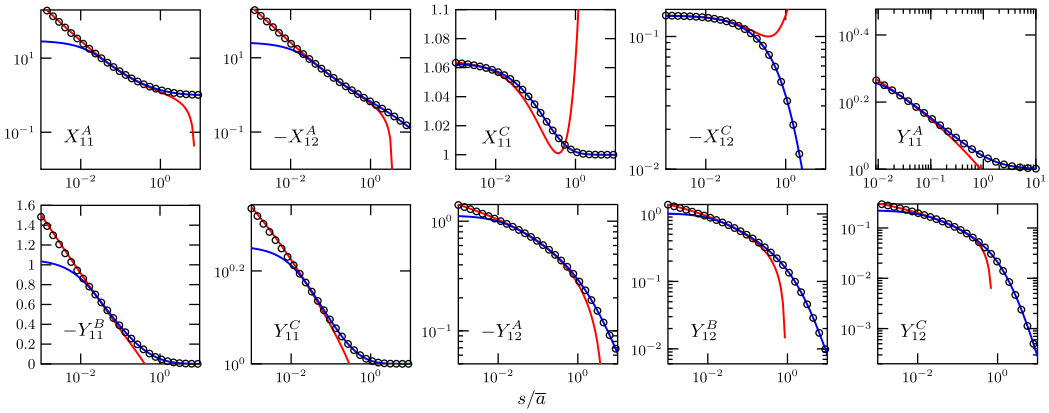

FIG. 2. Resistance functions against interfacial distances $s = R - a_1 - a_2$ for spheres with radius ratio $\lambda = 0.8$. Small-s asymptotes (red lines) and large-s asymptotes (blue lines) are from Ref. [38], while circles show the resistance functions matched between the small-s and large-s asymptotes using the procedure described in Sec. II.

the droplets, where $\overline{a} = (a_1 + a_2)/2$ denotes the mean droplet radius. Moreover, $\widehat{R}_j \equiv R_j/R$. In total there are 20 resistance functions in Eqs. (5): $X^A_{\alpha\beta}, Y^A_{\alpha\beta}, Y^B_{\alpha\beta}, X^C_{\alpha\beta}$, and $Y^C_{\alpha\beta}$, all with indices $\alpha, \beta = 1, 2$. Using the symmetries in Eqs. (3) and (4), only 10 of these are independent. Jeffrey and Onishi [38] computed them using a twin-multipole expansion, originally used by Jeffrey [39], to solve Laplace's equation. The resulting expressions obtained in the asymptotic regime of wide separations are illustrated in Fig. 2 for $\lambda = 0.8$. In the limit $R/\overline{a} \to \infty$, the components $X^A_{\alpha\alpha} = Y^A_{\alpha\alpha} = X^C_{\alpha\alpha} = Y^C_{\alpha\alpha} = 1$ for $\alpha = 1, 2$, and all other components are zero. The corresponding resistance tensors in Eqs. (5) are uncoupled between the particles: $A^{(\alpha\beta)}_{ij} = -6\pi\mu\overline{a}\delta_{\alpha\beta}\delta_{ij}$, $B^{(\alpha\beta)}_{ij} = \widetilde{\mathbb{B}}^{(\alpha\beta)}_{ij} = 0$, and $C^{(\alpha\beta)}_{ij} = -8\pi\mu\overline{a}^3\delta_{\alpha\beta}\delta_{ij}$. Here, each of the two particles undergo independent Stokes drag, with the force and torque of an isolated sphere in Stokes flow [8]:

$$\boldsymbol{F}^{(\alpha)}_{\mathrm{h}} = -6\pi\mu a_\alpha \boldsymbol{v}^{(\alpha)}, \tag{6a}$$

$$\boldsymbol{T}^{(\alpha)}_{\mathrm{h}} = -8\pi\mu a^3_\alpha \boldsymbol{\omega}^{(\alpha)}. \tag{6b}$$

The timescale $\tau_{\mathrm{p},\alpha} = m_\alpha/(6\pi\mu a_\alpha)$ defines the Stokes damping time of individual droplets.

Jeffrey and Onishi [38] also computed the resistance functions for nearly touching spheres. However, the results in this limit contained a number of errors that were corrected by Townsend [40]. We used these corrected functions in our model. In order to verify that these corrections provide consistent approximations for the hydrodynamic forces and torques, we made the following two checks. First, for all 10 functions, we summed the expansions derived by Jeffrey and Onishi [38] for large separations, including 150, 200, 250, and 300 terms, and confirmed that the results matched smoothly with the asymptotes at small separations for radius ratios larger than 0.1. This matching is shown in Fig. 2 for $\lambda = 0.8$. Second, we compared to results for the radial and tangential mobility functions of Ref. [12], based upon the series solutions for widely separated, noninertial spheres in Ref. [41]. We inverted Eq. (2), and set hydrodynamic forces and torques to zero, to obtain the mobility functions for droplets in the limit of zero inertia. We confirmed that our results matched the functions L and M shown in Figs. 5 and 9 of Ref. [12]. This is an independent check that our resistance functions are correctly implemented.

When the interfacial distance $s = R - a_1 - a_2$ between two droplets is comparable to the mean-free path ℓ of air, the hydrodynamic approximation breaks down, meaning that the expressions for $\boldsymbol{F}^{(\alpha)}_{\mathrm{h}}$ and $\boldsymbol{T}^{(\alpha)}_{\mathrm{h}}$ above are no longer valid. Instead, the droplets move in a noncontinuum flow described by the Boltzmann equation. The resulting noncontinuum corrections to the radial

hydrodynamic forces between two spheres were first computed by Sundararajakumar and Koch [10]. They used solutions to the linearized Boltzmann equation to calculate the noncontinuum radial resistance functions for interfacial distances smaller than the mean-free path. The corresponding tangential corrections were evaluated by Li Sing How *et al.* [9]. In our numerical computations we used the uniformly valid resistance functions (denoted by the superscript uv) quoted in Ref. [42], their Eqs. (4.12) to (4.15):

$$X^{A,\mathrm{uv}}_{\alpha\beta} = X^{A}_{\alpha\beta} + (-1)^{\alpha+\beta}\frac{a_1a_2}{\overline{a}(a_\alpha+a_\beta)}\left(\frac{f^{\parallel}_{\mathrm{fit}}}{\mathrm{Kn}} - \frac{\overline{a}}{R-2\overline{a}}\right), \tag{7a}$$

$$Y^{A,\mathrm{uv}}_{\alpha\beta} = Y^{A}_{\alpha\beta} + (-1)^{\alpha+\beta}\frac{a_1a_2}{\overline{a}(a_\alpha+a_\beta)}\left[\frac{1}{3\sqrt{\pi}}\widetilde{W} + \left(\frac{1-\lambda}{1+\lambda}\right)^2\widetilde{Q}\right], \tag{7b}$$

$$Y^{B,\mathrm{uv}}_{\alpha\beta} = Y^{B}_{\alpha\beta} + 2\frac{a_1a_2}{\overline{a}(a_\alpha+a_\beta)}\left(\frac{a_\alpha}{\overline{a}}\right)^{|\alpha-\beta|}\left[\frac{(-1)^\beta}{4\sqrt{\pi}}\widetilde{W} - (-1)^{(\alpha+\beta)}\frac{3}{4}\frac{1-\lambda}{1+\lambda}\widetilde{Q}\right], \tag{7c}$$

$$Y^{C,\mathrm{uv}}_{\alpha\beta} = Y^{C}_{\alpha\beta} + \frac{a_1a_2}{\overline{a}(a_\alpha+a_\beta)}\left(\frac{a_1a_2}{\overline{a}^2}\right)^{|\alpha-\beta|}\left[\frac{1}{4\sqrt{\pi}}\widetilde{W} + (-1)^{(\alpha+\beta)}\frac{3}{4}\widetilde{Q}\right]. \tag{7d}$$

The above equations describe corrections to 16 out of the 20 resistance functions mentioned above. The radial rotational resistance function $X^{C}_{\alpha\beta}$ is not modified [42]. In the above equations, $\mathrm{Kn} = \ell/\overline{a}$ is the Knudsen number and $\overline{a}$ is the mean droplet radius. The functions $f^{\parallel}_{\mathrm{fit}}$, $\widetilde{W}$, and $\widetilde{Q}$ are quoted in the Appendix. The corrections in Eqs. (7) are computed using the linearized Boltzmann equation, valid when the Mach number remains small. An additional simplification is that the collision term in the Boltzmann equation is replaced by a collision operator which relaxes the molecular velocity to a Maxwellian distribution [43], leading to an approximation to the Boltzmann equations which allows analytical solutions. Finally, the results in Eqs. (7) are valid in the asymptotic limit $\mathrm{Kn} \to 0$.

In summary, to evaluate the hydrodynamic force and torque between two droplets in Eq. (2), we use the resistance matrices in Eqs. (5) based on the uniformly valid resistance functions $X^{\mathrm{uv}}_{\alpha\beta}$ and $Y^{\mathrm{uv}}_{\alpha\beta}$ in Eqs. (7), with $X_{\alpha\beta}$ and $Y_{\alpha\beta}$ evaluated using the asymptotes shown in Fig. 2. The asymptotes are matched at the location where their difference is smallest.

The resistance tensors $\mathbb{B}^{(\alpha\beta)}$ and $\widetilde{\mathbb{B}}^{(\alpha\beta)}$ coupling translations and rotations in Eq. (2) are subleading in $1/R$ compared to the translational resistance tensors $\mathbb{A}^{(\alpha\beta)}$ and $\mathbb{C}^{(\alpha\beta)}$ [8]. When the droplets are far apart, their angular velocities may therefore be neglected, as in Ref. [34]. However, for droplets traveling at small interfacial distances, the angular dynamics must be considered because hydrodynamic torques tend to cause one droplet to roll over the other one.

C. Electrostatic force

We assume that the timescale at which charges redistribute on the droplets is much smaller than the shortest timescale of the relative droplet dynamics. In this limit, the droplets can be considered as good conductors. Lekner [35] derived expressions for the electrostatic force between two charged conducting spheres. The resulting expressions are valid for arbitrary separations between the spheres in a dielectric medium, with the assumption that the droplets do not deform. We outline the main steps of the derivation in Ref. [35] here, and discuss the details of when this model applies in Sec. IV.

The electrical potential energy $\mathscr{W}$ of two conductors with charges q_α and potentials $\mathscr{V}_\alpha$ is given by

$$\mathscr{W} = \frac{k_{\mathrm{e}}}{2}\left(q_1\mathscr{V}_1 + q_2\mathscr{V}_2\right), \tag{8}$$

where k_{e} is the Coulomb constant. The charges are linearly related to the electrical potentials

$$\begin{bmatrix} q_1 \\ q_2 \end{bmatrix} = \begin{bmatrix} C_{11} & C_{12} \\ C_{21} & C_{22} \end{bmatrix}\begin{bmatrix} \mathscr{V}_1 \\ \mathscr{V}_2 \end{bmatrix}, \tag{9}$$

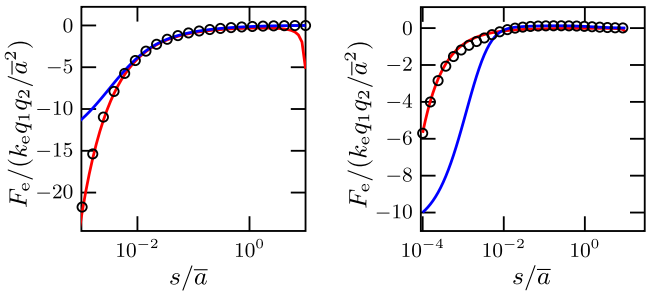

FIG. 3. Comparison of asymptotes for the electrostatic force F_e at interfacial distances $s = R - a_1 - a_2$ much smaller than $a_1 + a_2$ ($F_{e,near}$,red) and much larger ($F_{e,far}$,blue) for droplets with opposite charges $q = \pm 20\,000e$ (left) and same charges $q = 20\,000e$ (right). Circles show the smoothed force $F_{e,uv}$ in Eq. (12) with $s_m = 0.02$ (opposite charges) and $s_m = 0.01$ (same charges). Parameters $\lambda = 0.8$.

with capacitance coefficients $C_{\alpha\beta}$ [44]. The capacitance coefficients depend on the radii of the spheres a_1 and a_2, and upon the center-of-mass distance R between them as follows [45]:

$$C_{11} = a_1 a_2 \sinh(U) \sum_{n=0}^{\infty} \{a_1 \sinh(nU) + a_2 \sinh[(n+1)U]\}^{-1}, \tag{10a}$$

$$C_{22} = a_1 a_2 \sinh(U) \sum_{n=0}^{\infty} \{a_2 \sinh(nU) + a_1 \sinh[(n+1)U]\}^{-1}, \tag{10b}$$

$$C_{12} = C_{21} = -a_1 a_2 \frac{\sinh(U)}{R} \sum_{n=1}^{\infty} [\sinh(nU)]^{-1}, \tag{10c}$$

with $U = \operatorname{acosh}[(R^2 - a_1^2 - a_2^2)/(2a_1 a_2)]$. Eliminating the potentials in Eq. (8) by means of Eqs. (9) and (10), one obtains the electrostatic potential energy $\mathscr{W}$. For well-separated droplets, $R \gg a_1 + a_2$, the lowest-order nonconstant contribution simplifies to the Coulomb energy between point charges $\mathscr{W} \sim k_e q_1 q_2 / R$. Moreover, by differentiation of $\mathscr{W}$ with respect to R one obtains the electrostatic force F_e. Truncating the sums in Eqs. (10) allows us to compute the electrical force when droplets are far apart. In the numerical experiments discussed in this paper, we included terms up to $n = 30$ to calculate the asymptotic electrostatic force $F_{e,far}$. When $R \gg a_1 + a_2$, the sums in Eq. (10) converge rapidly. When the center-of-mass distance is close to $a_1 + a_2$, however, this is not the case. Lekner derived an approximate expression for the force between perfectly conducting spheres, valid at interfacial distance $s = R - a_1 - a_2$, much smaller than the droplet size, Eq. (3.4), in Ref. [35]:

$$F_{e,near} = -k_e \frac{a_1 + a_2}{a_1 a_2 s} \frac{\left[\left(\psi\left(\frac{1}{1+\lambda}\right) + \gamma\right) q_2 - \left(\psi\left(\frac{\lambda}{1+\lambda}\right) + \gamma\right) q_1\right]^2}{\left[\left(\psi\left(\frac{1}{1+\lambda}\right) + \gamma\right)\left\{2\gamma + \ln\left[\frac{2a_1 a_2}{(a_1+a_2)s}\right]\right\} + \left(\psi\left(\frac{\lambda}{1+\lambda}\right) + \gamma\right)\left\{-2\psi\left(\frac{1}{1+\lambda}\right) + \ln\left[\frac{2a_1 a_2}{(a_1+a_2)s}\right]\right\}\right]^2}. \tag{11}$$

Here $\psi(x)$ is the digamma function, and $\gamma = 0.5772\ldots$ is Euler's constant. In order to obtain an approximation valid uniformly in R, we match the two asymptotes at the interfacial distance s_m where the absolute difference between the two asymptotes reaches a minimum, using exponential smoothing of the form

$$F_{e,uv} = F_{e,near}\, e^{-s/s_m} + F_{e,far}\,(1 - e^{-s/s_m}). \tag{12}$$

The asymptotes for small and large interfacial distances are shown in Fig. 3 for one set of parameters. We confirmed that this matching procedure works for the parameter ranges considered

in this paper. However, we expect that higher-order corrections to $F_{\mathrm{e,near}}$ must be included for charge ratios outside the range $0.1 < |q_1/q_2| < 10$.

D. Nondimensional numbers

To find a set of nondimensional parameters governing the collision dynamics, we nondimensionalize the dynamics in Eq. (1) as follows. As a length scale we use $\overline{a} = (a_1 + a_2)/2$. Velocities are nondimensionalized with the differential settling speed of noninteracting droplets, $V_0 = g|\tau_{\mathrm{p},1} - \tau_{\mathrm{p},2}|$, where $\tau_{\mathrm{p},\alpha}$ is the Stokes damping time of droplet α. Time is nondimensionalized with the timescale at which freely settling droplets pass each other $\tau_{\mathrm{c}} = \overline{a}/V_0$. The resulting dynamics is governed by five nondimensional parameters. First, particle inertia is characterized by the Stokes number $\mathrm{St} = \widetilde{\tau}_{\mathrm{p}}/\tau_{\mathrm{c}}$, where $\widetilde{\tau}_{\mathrm{p}} = \widetilde{m}/(6\pi\mu\overline{a})$ and $\widetilde{m} = (4/3)\pi\overline{a}^3\varrho_{\mathrm{w}}$ are the relaxation timescale and droplet mass based on the mean droplet radius $\overline{a}$. Second, the Coulomb number $\mathrm{Cu} = 2k_{\mathrm{e}}|q_1q_2|/[\widetilde{m}(a_1 + a_2)V_0^2]$ is the ratio of the Coulomb energy upon contact and kinetic energy $\widetilde{m}V_0^2/2$. Related parameters (ratio of Coulomb to average thermal kinetic energy) were used by Hidy and Brock [46] to quantify the effect of electric charge on Brownian coagulation, and in Refs. [34,47–49] to parametrize the importance of charge on the dynamics of micron-sized water droplets in turbulent air. The remaining three nondimensional parameters are the Knudsen number $\mathrm{Kn} = \ell/\overline{a}$, the ratio of the mean-free path of air ℓ to the mean droplet radius, the radius ratio $\lambda = a_1/a_2$, and the charge ratio $\lambda_q = q_1/q_2$. The charge ratio can take positive or negative values, depending on the polarities of the excess charge on the droplets.

E. Numerical integration

To make sure that droplets do not overlap in the numerical simulations when they travel at very small interfacial distances s for finite times, we followed Ref. [42] and employed a fourth-order Runge-Kutta algorithm with an adaptive time step. Our prescription for the adaptive time step differs slightly from the one in Ref. [42]. We used $\Delta t = \varepsilon \min\{s/|V_R|, s/|V_T|\}$. Here, V_R and V_T are the radial and tangential relative velocities, and $\varepsilon \ll 1$ is a numerical constant. The numerical results shown in Fig. 4 were obtained for $\varepsilon = 0.08$. We verified that reducing the numerical constant to $\varepsilon = 0.001$ did not change the results shown in Fig. 4(d).

We recorded a collision and stopped the numerical integration as soon as the interfacial distance became smaller than 10^{-8} μm. We verified that using a larger cutoff, 10^{-7} μm, did not change the results shown in Fig. 4(d).

III. RESULTS

The collision efficiency $\mathscr{E}$ is defined in terms of the critical impact parameter b_{c} beyond which droplet pairs with initial large vertical separation cease to collide, $\mathscr{E} = b_{\mathrm{c}}^2/(a_1 + a_2)^2$. The impact parameter and, consequently, the collision efficiency are influenced by hydrodynamic interactions as well as by electric charges carried by the droplets. In the following we discuss how the collision efficiency depends on the excess droplet charge. For droplets charged with equal and with opposite polarities, we describe a transition at a critical charge q_{c}, from a regime at small charges that is dominated by noncontinuum effects, to a charge-dominated regime at large excess charges. The collision efficiency is determined by a high-dimensional saddle point of the relative dynamics below the collision sphere, and we determine q_{c} as the charge where this saddle point leaves the region where noncontinuum effects dominate [Fig. 1(b)]. Our results for the collision efficiency are shown in Fig. 4 for droplets that carry the same amount of charge with different polarities (left), or with the same polarity (right). We discuss these two cases separately in Secs. III A and III B.

The droplets were initialized far apart in the $R_1 - R_3$ plane, with initial velocities of independently settling droplets in still air. Since there were no transversal forces between the droplets, the dynamics remained constrained to the $R_1 - R_3$ plane. In addition, the only nonzero component of the droplets angular velocities was $\omega_2^{(\alpha)}$. In summary, for each particle one component of the

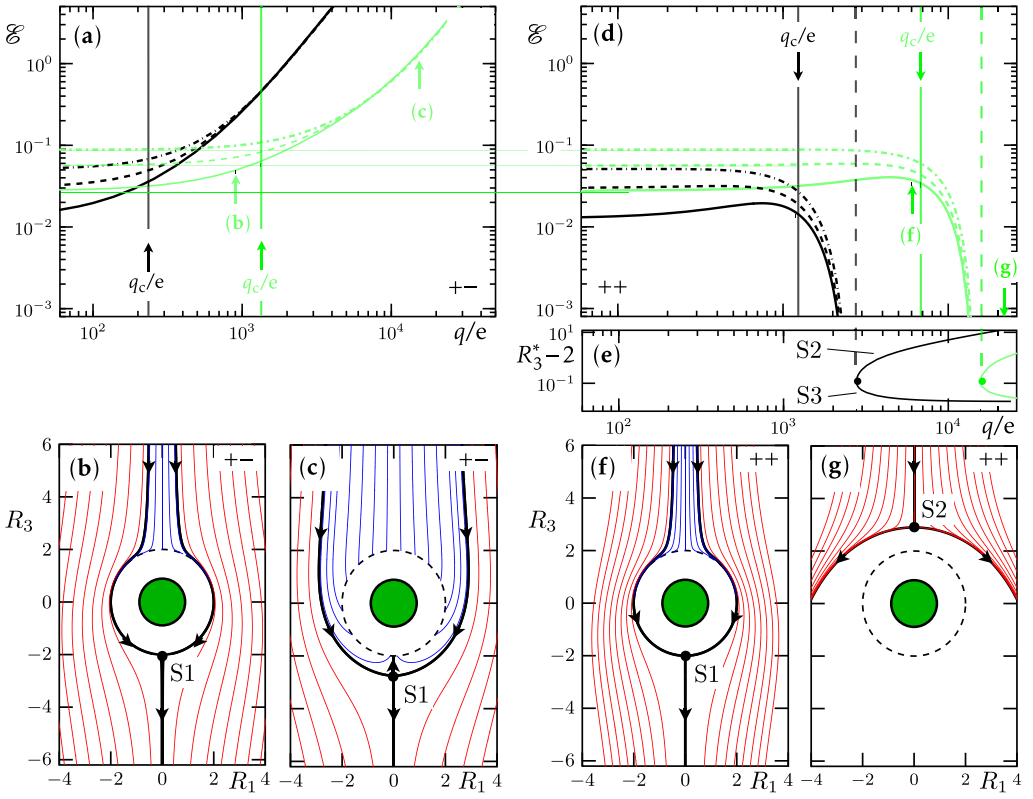

FIG. 4. Collision efficiencies and phase portraits of charged droplets settling in still air, following the model in Sec. II. (a) Collision efficiency $\mathcal{E}$ for droplets with equal amounts of charge of opposite polarity, as a function of charge $q = |q_\alpha|$, with $\alpha = 1, 2$ over elementary charge e. Droplet radii: $a_1 = 16\,\mu$m and $a_2 = 20\,\mu$m (green), and $a_1 = 8\,\mu$m and $a_2 = 10\,\mu$m (black). Kn $= 10^{-3}$ (solid lines), 10^{-2} (dashed), and 5×10^{-2} (dashed-dotted). The vertical solid lines indicate the locations where Eqs. (16) and (17) predict a transition for Kn $= 10^{-3}$. Arrows denote the charges in (b) and (c). Horizontal lines show the $q \to 0$ asymptotes for the larger droplet pair. (b) Shows the relative droplet dynamics in the $R_1 - R_3$ plane (where R_i is nondimensionalized by $\bar{a}$), for $a_1 = 16\,\mu$m, $a_2 = 20\,\mu$m, $q = 908\,e$, and Kn $= 10^{-3}$. Colliding trajectories (blue), noncolliding trajectories (red). The solid black line is the separatrix between colliding and noncolliding trajectories, and • represents the saddle point S1. (c) Same as (b), but for $q = 15469\,e$. Manifolds of the saddle point S1 (•) are shown as black solid lines. (d) Same as (a), but for equal polarity. (e) Shows the bifurcations (their locations $q_{c,2}$ are denoted by vertical dashed lines) that give rise to saddle points S2 and S3. (f) Shows the relative dynamics in the $R_1 - R_3$ plane for $a_1 = 16\,\mu$m, $a_2 = 20\,\mu$m, $q = 6011\,e$ along with the saddle point S1, and (g) corresponds to $q = 21199\,e$, and shows the saddle point S2.

droplet velocities and two components of angular velocities remained zero throughout the numerical experiments, $v_2^{(\alpha)} = 0$, $\omega_1^{(\alpha)} = 0$, and $\omega_3^{(\alpha)} = 0$.

A. Opposite charges

Figure 4(a) shows that electrostatic attraction increases the collision efficiencies $\mathscr{E}$ for droplet pairs of radii 8 and 10 μm (black) more strongly than for droplets with radii 16 and 20 μm (green). The droplets were charged with the same amount of excess charge, but with different polarities. For charges weaker than the critical charge, $\mathscr{E}$ is approximately independent of charge, but the collision efficiency depends on the Knudsen number Kn [see different line styles in Fig. 4(a)]. In this limit,

the collision dynamics resembles that of neutral droplets settling in still air [34] (but note that there are subtle differences that we discuss below). For charges larger than the critical charge, by contrast, the collision efficiency is independent of Kn, as explained by Magnusson *et al.* [34]. The difference between these two regimes can be understood by following the collision dynamics in the $R_1 - R_3$ plane [Fig. 1(a)], corresponding to the rest frame of the smaller droplet.

Consider first the limit of large charges, Fig. 4(c). This panel shows the relative trajectories of droplets at a fixed charge larger than the critical charge q_c. In this case, the collision efficiency is determined by the stable manifold of a saddle point S1 located on the R_3 axis below the collision sphere. The unstable manifold of the saddle is one dimensional, with a component along the R_3 axis. The stable manifold therefore has codimension one. As a consequence, the stable manifold forms a separatrix for the phase-space dynamics [50]. The set of initial conditions of independently settling droplets at the critical impact parameters $\pm b_c$ defines two one-dimensional trajectories on the stable manifold. These are projected onto the $R_1 - R_3$ plane and shown as solid black trajectories ending at S1 in Fig. 4(c). All trajectories that approach the collision sphere starting within the space enclosed by these trajectories must collide (blue) with the collision sphere. All other trajectories do not collide (red). Four of the stable eigenvalues of S1 are complex, allowing phase-space trajectories to spiral around this fixed point. Indeed, we observe that the trajectories plotted in black in Fig. 4(c) do slightly overshoot the saddle point S1, but this is not visible in the figure. Since the saddle point and its stable manifold are far from the collision sphere, the local breakdown of the hydrodynamic approximation does not matter. As a consequence, the collision efficiency is independent of Kn. This is the limit analyzed by Magnusson *et al.* [34]. Their model included only leading-order corrections in $1/R$ to hydrodynamic interactions and ignored the breakdown of the hydrodynamic approximation near contact.

The limit of small charges, shown in Fig. 4(b), is more subtle than the large-charge limit. As mentioned above, the collision dynamics looks like that for neutral droplets, where the separatrices delineating collisions from no collisions (solid black trajectories entering from above) are grazing trajectories. However, our numerics indicates that separatrices shown in Fig. 4(b) do not graze the collision sphere. They lie very close to the collision sphere, and appear to connect to the saddle point S1 mentioned in the previous paragraph, which now occurs very close to the collision sphere. The numerical integration becomes difficult when the trajectory travels along the collision sphere at interfacial distances s smaller than the mean-free path ℓ. Therefore, we could not resolve the saddle point in the numerical integration (the trajectories corresponding to the separatrices do not hit the saddle point, but they pass very close to it).

As outlined above, a transition between the two different regimes shown in Fig. 1(b) occurs when the saddle point S1 exits the region $s < \ell$. In order to compute the charge q_c at which the transition occurs, we start by determining the location of the saddle points of the relative droplet dynamics for $\boldsymbol{R} = \boldsymbol{x}^{(2)} - \boldsymbol{x}^{(1)}$ and $\boldsymbol{V} = \boldsymbol{v}^{(2)} - \boldsymbol{v}^{(1)}$. At the saddle point, $\dot{\boldsymbol{R}} = 0$, implying that the droplets fall at a constant separation $\boldsymbol{R}^*$, with vanishing relative velocity $\boldsymbol{V}^* = 0$. The latter condition implies a common steady-state settling velocity $\boldsymbol{v}^{(1)} = \boldsymbol{v}^{(2)} = \boldsymbol{v}_s^*$. Due to the symmetry of the problem, both $\boldsymbol{v}_s^*$ and $\boldsymbol{R}^*$ must point along the direction of gravity, $\boldsymbol{v}_s^* = -v_s^* \hat{R}_3$ and $\boldsymbol{R}^* = -R^* \hat{R}_3$, where v_s^* and R^* are the components in the gravity direction, and $\hat{R}_3$ is the unit vector in the R_3 direction. Since there is no external torque acting on the droplets, and because of the dissipative nature of the dynamics, the angular velocities at the saddle point must vanish, $\boldsymbol{\omega}^{(\alpha)} = 0$. What remains is to calculate v_s^* and R^* from the condition that $\dot{v}_3^{(\alpha)} = 0$ in Eq. (1b) at the steady state [34]

$$F_{g,3}^{(\alpha)} + F_{h,3}^{(\alpha)} + F_{e,3}^{(\alpha)} = 0 \quad \text{for} \quad \alpha = 1, 2. \tag{13}$$

Given the forces described in Sec. II, Eq. (13) simplifies to

$$-m_1 g + 6\pi\mu \left(a_1 X_{11}^{A,\mathrm{uv}} + \overline{a} X_{12}^{A,\mathrm{uv}} \right) v_s^* + F_e = 0, \tag{14a}$$

$$-m_2 g + 6\pi\mu \left(a_2 X_{22}^{A,\mathrm{uv}} + \overline{a} X_{21}^{A,\mathrm{uv}} \right) v_s^* - F_e = 0. \tag{14b}$$

Here the resistance coefficients $X^A_{\alpha\beta}$ and $F_e = F^{(1)}_{e,3}$ are functions of R^*. For given droplet radii and charges, solutions to these equations give the saddle-point location R^* on the R_3 axis, and center-of-mass settling speed v^*_s. For the parameters corresponding to Fig. 4(b), we find the nondimensional interfacial distance at the saddle point $s^* = R^* - 2\bar{a} \approx 6 \times 10^{-4}\bar{a}$. So the equilibrium point is very close to, but not on, the collision sphere. Numerical evaluation of the stability exponents shows that it is a saddle point with both stable and unstable eigendirections. However, as mentioned above, we could not find the stable and unstable manifolds by numerical integration because this becomes hard close to the collision sphere. As the charge tends to zero, the saddle approaches the collision sphere $R^* \to 2\bar{a}$. Conversely, as the charge increases, the saddle moves down the R_3 axis. We conclude that the saddle point identified in Ref. [34] appears already at small Coulomb numbers, $\mathrm{Cu} \ll 1$. Since the numerical integration is more difficult at charges smaller than those shown in Figs. 4(a) and 4(d), we did not investigate this limit by numerical integration.

How much charge is needed to cross over from the small charge limit where noncontinuum effects determine collisions to the charge-dominated limit? There is no bifurcation, the same saddle point determines the collision dynamics in both regimes. But the above considerations indicate that the transition occurs when the saddle point leaves the region $s < \ell$ in the $R_1 - R_3$ plane, the hashed region in Fig. 1(b). If the saddle point is close to the collision sphere, its location and its manifolds depend on Kn. By contrast, when the interfacial separation at the saddle point is much larger than the mean-free path, $s \gg \ell$, the saddle point and its associated separatrix are independent of Kn, and the collision efficiency is determined by electrostatic forces.

To find the critical charge q_c, we set the interfacial separation at the saddle point equal to the mean-free path ℓ in Eqs. (14). Substituting $s^* = \ell$ into Eqs. (14) and solving for v^*_s and F_e we find the electrostatic force required to maintain a time-independent relative settling velocity v_s:

$$v_s = \frac{4a_1^2 g\varrho_w(1+\lambda^3)}{9\mu\lambda^2}\frac{1}{2\lambda X^{A,uv}_{11} + (1+\lambda)\left(X^{A,uv}_{12} + X^{A,uv}_{21}\right) + 2X^{A,uv}_{22}}, \tag{15a}$$

$$F_e = \frac{4a_1^3 g\pi\varrho_w}{3\lambda^3}\frac{-2\lambda X^{A,uv}_{11} - (1+\lambda)X^{A,uv}_{12} + \lambda^3\left[(1+\lambda)X^{A,uv}_{21} + 2X^{A,uv}_{22}\right]}{2\lambda X^{A,uv}_{11} + (1+\lambda)\left(X^{A,uv}_{12} + X^{A,uv}_{21}\right) + 2X^{A,uv}_{22}}. \tag{15b}$$

To determine the corresponding amount of charge, we approximate F_e and the resistance functions by their asymptotes at small interfacial distances (Sec. II) and solve Eq. (15b). We find

$$|q_1 q_2| = \frac{1}{h(\lambda,\lambda_q)} \times \frac{a_2^5\lambda^4 g\varrho_w \mathrm{Kn}}{k_e}\left[f^{(1)}(\lambda)\ln\left(\frac{4\lambda}{(1+\lambda)^2\mathrm{Kn}}\right)^2 + f^{(2)}(\lambda)\ln\left(\frac{4\lambda}{(1+\lambda)^2\mathrm{Kn}}\right) + f^{(3)}(\lambda)\right]. \tag{16}$$

In this expression, the function $h(\lambda, \lambda_q)$ is defined as

$$h(\lambda,\lambda_q) = \frac{1}{|\lambda_q|}\left\{\left[\psi\left(\frac{1}{1+\lambda}\right) + \gamma\right] - \left[\psi\left(\frac{\lambda}{1+\lambda}\right) + \gamma\right]\lambda_q\right\}^2. \tag{17a}$$

The expressions for the functions $f^{(k)}$ are quite lengthy. Their full forms are plotted in Fig. 5. Here we only quote their Padé approximants around $\lambda = 1$, of order [3,3] (the transition values shown in Fig. 4 were obtained using the full forms):

$$f^{(1)} = \frac{8.98831(\lambda-1) - 12.553(\lambda-1)^2 + 4.18158(\lambda-1)^3}{1 - 3.39659(\lambda-1) + 3.95407(\lambda-1)^2 - 1.59769(\lambda-1)^3}, \tag{17b}$$

$$f^{(2)} = \frac{-45.6737(\lambda-1) + 2.16728(\lambda-1)^2 - 0.229416(\lambda-1)^3}{1 + 1.95255(\lambda-1) + 0.830927(\lambda-1)^2 - 0.112841(\lambda-1)^3}, \tag{17c}$$

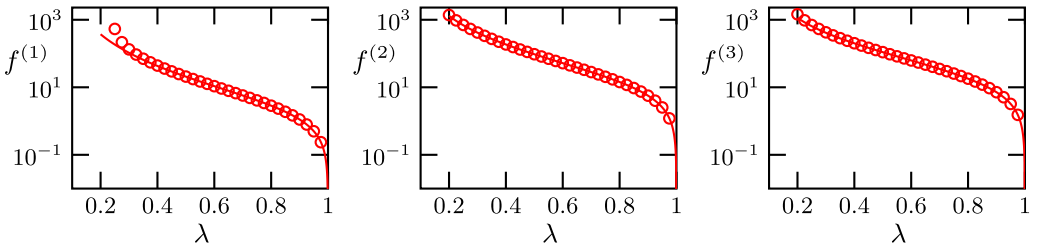

FIG. 5. The full forms of the functions $f^{(k)}$ with $k = 1, 2, 3$ in Eq. (16) (lines) and their order [3,3] Padé approximants around $\lambda = 1$, Eqs. (17) (circles).

$$f^{(3)} = \frac{-58.0221(\lambda-1) - 5.79319(\lambda-1)^2 - 2.67774(\lambda-1)^3}{1 + 2.09984(\lambda-1) + 1.39178(\lambda-1)^2 + 0.352657(\lambda-1)^3}. \tag{17d}$$

Figure 4(a) shows the predicted critical charge $q_c = |q_\alpha|$ for droplets with equal charge magnitude but opposite polarities ($\lambda_q = -1$), computed using Eqs. (16) and (17) as vertical solid lines. We see that the theory predicts the transition from the small-charge limit where noncontinuum effects determine collisions to the charge-dominated regime for both droplet sizes considered. This confirms the theoretical prediction that the transition occurs when the saddle point leaves the Kn-dominated region in the $R_1 - R_3$ plane. Figure 6(a) shows how the predicted critical charge q_c depends on a_2 at fixed λ (red crosses). Equation (16) says that this charge depends on the droplet size as $q_c \sim a_2^{5/2}$, which matches the numerical results (red circles) shown in Fig. 6(a). These numerical results were obtained by plotting the collision efficiency as a function of charge, similar to Fig. 4(a), for different values of a_2 and then finding the intersection of the large-charge asymptote to the small-charge asymptote.

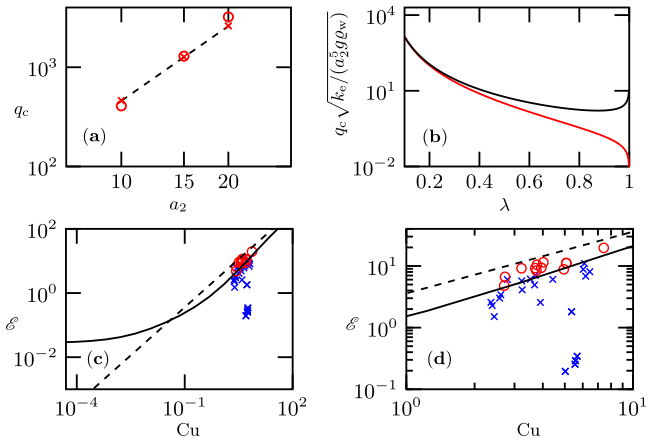

FIG. 6. (a) Critical charge q_c as a function of size of the larger droplet a_2 for three values of $a_2 = 10$, 15, and 20 µm, Kn = 0.01, $\lambda = 0.8$ in our simulations (red circles) compared to the theory in Eq. (16) (red crosses). The dashed line is a guide to the eye. (b) Theoretical prediction (16) for the critical charge against radius ratio λ of droplets with equal amounts of charge q_c with same polarity $\lambda_q = 1$ (black) and opposite polarity $\lambda_q = -1$ (red), and Kn = 10^{-3}. The critical charge q_c is nondimensionalized by $(a_2^5 g\varrho_w/k_e)^{1/2}$. The nondimensional charge remains a function of λ, λ_q, and Kn. (c) Collision efficiency $\mathscr{E} = b_c^2/(a_1 + a_2)^2$ against Coulomb number (Cu) from Fig. 4(a) (black line) for Kn = 10^{-3}. Equation (4) from Ref. [30] is shown as a dashed line. The markers show $b^2/(a_1 + a_2)^2$ from the experimental data in Ref. [34] of passing droplet pairs with different impact parameters b that either collide (blue crosses) or miss (red circles). (d) Zoom-in of (c).

Figure 6(b) shows the dependence of the nondimensional critical charge against particle radius ratio λ for small Kn. For droplets of opposite polarity, the critical charge approaches zero as λ approaches unity, while for λ deviating from unity, the amount of charge required to balance differential settling at the saddle point increases. As found above, the critical charge is one order of magnitude larger for droplets of the same polarity when $\lambda \sim 0.8$. This separation becomes even larger and diverges as λ approaches unity. For small λ, however, the critical charge is of the same order for equal and opposite polarities.

Finally, we validate the model predictions by comparing them against experimental observations. Reference [34] presented collision efficiencies of oppositely charged water droplets with radius ratio approximately 0.8 where the droplet sizes varied between 17 to 25 μm. In Figs. 6(c) and 6(d) we compared these experiments to model simulations for droplets of sizes 16 and 20 μm. We see that our model describes the boundary between collisions and noncollisions well. By contrast, the parameter-fitted equation described in Ref. [30] predicts a collision efficiency larger than that observed experimentally.

B. Same charges

Figure 4(d) illustrates that the collision efficiencies $\mathscr{E}$ for droplet pairs with equal amounts of excess positive charge tend to zero as the charge increases. Coulomb repulsion prevents collisions entirely at sufficiently large charges. Furthermore, the collision efficiency vanishes more quickly for the droplet pair with radii 8 and 10 μm than for the droplet pair with radii 16 and 20 μm, as expected, because the Coulomb number is larger for smaller droplets with the same charge. As in Fig. 4(a), we identify two regimes. For small charges, the collision efficiency depends on Kn but the Kn dependence becomes much weaker as the charge magnitude increases and the collision efficiency becomes charge dominated. The transition mechanism is the same as for oppositely charged droplets: despite the fact that the droplets carry charges with the same polarity, the electrostatic force is attractive at small separations due to extreme polarization of the droplet charges [35]. This gives rise to a saddle-point S1 below the collision sphere [Fig. 4(f)], where the attractive force balances differential settling. The corresponding predictions of Eq. (16) with $\lambda_q = +1$ are shown as vertical solid lines in Fig. 4(d). One difference to the collision dynamics for charged droplets with opposite polarity [Fig. 4(a)] is that the crossover between the small-charge regime where noncontinuum effects determine collisions and the charge-dominated regime occurs at much larger charges in Fig. 4(d). The reason for this difference is that the small-s attractive electrical force (11) between droplets with the same charge magnitude is weaker than the attractive force for droplets with opposite charges, implying that larger charge magnitudes are required in order to balance the right-hand side in Eq. (15b), where the saddle point reaches $s = \ell$. Moreover, the electrostatic force for droplets with the same charge is repulsive at large interfacial distances. Since the force attracts at small separations, it must change sign at a critical distance s_c that depends on λ and λ_q. Therefore, the droplet interfacial separation at the saddle point must remain smaller than this critical distance s_c, as the charge increases. For the parameters used here, $s_c \approx 0.018\bar{a}$. This means that the collision efficiency for droplets with the same polarity becomes independent of the Kn number only when $\mathrm{Kn} < 0.018$. There is no such condition for droplets charged with opposite charges because the saddle point continues to move down as the amount of charge increases (Sec. III A).

As the magnitude of the excess charge increases, a bifurcation at $q_{c,2}$ gives rise to two new saddle points, S2 and S3 on the R_3 axis above the collision sphere. The saddle point S2 results from the balance between electrostatic repulsion and differential settling. In contrast to S1, the unstable manifold of S2 is two dimensional, implying that its stable manifold cannot form a separatrix for the collision dynamics by dividing the phase space into disjoint sets [50]. Despite this, for the droplet sizes and initial conditions considered, we do not observe any collisions for charges larger than $q_{c,2}$. The values of $q_{c,2}$ are shown in Fig. 4(d) as dashed vertical lines. Interestingly, we also observe that $\mathscr{E}$ tends to become vanishingly small well before the bifurcation occurs. The reason is that

even before the saddle point appears, the dynamics in the R_3 direction slows down in its vicinity. These slow trajectories are then deflected in the unstable R_1 direction so that only trajectories approaching infinitesimally close to the R_3 axis can collide. We hypothesize that the qualitative form of the collision rate before the bifurcation can be understood by studying the normal form of the bifurcation for our system.

The second fixed point S3 lies below S2 and is shielded by it from above. Its unstable manifold is three dimensional. This saddle point is not approached by trajectories starting at large separations for the Stokes numbers considered here. However, at much larger Stokes numbers, trajectories could overshoot the saddle S2 and approach the fixed point S3. We determined the charge $q_{c,2}$ at which the bifurcation leading to the appearance of S2 and S3 occurs by numerically solving Eq. (14) for $\boldsymbol{R}^* = [0, 0, R_3^*]^\mathsf{T}$ with $R_3^* > 0$ and the common settling speed v_s^*. We determined the location of the bifurcation by computing the value of the droplet charge for which Eq. (14) had exactly one solution for $R_3 > 0$. The locations of the two saddles on the R_3 axis, for $R_3 > 0$, are shown in Fig. 4(e). Figure 4(f) shows the relative dynamics in the $R_1 - R_3$ plane before bifurcation. It is qualitatively similar to panel Fig. 4(b). At charges weaker than the critical charge $q_{c,2}$, it does not matter whether the droplets have the same or opposite polarities. Figure 4(g) shows the case where the charge is larger than $q_{c,2}$, showing that the unstable manifolds of the saddle point S2 block collisions. For both cases, the saddle point S1 exists below the collision sphere due to the attractive force at close approach.

IV. DISCUSSION

The amount of excess charge required to reach the Coulomb-dominated collision regime depends on whether the two droplets have excess charges of the same sign, or not. For droplets carrying the same charges, larger amounts of charge are required to qualitatively change the collision dynamics, about $q_c \sim 10^4\, e$ for droplets with radii 16 and 20 μm as observed from Fig. 4. For droplets that are charged with opposite polarities, much smaller charges are required, about $10^3\, e$ for droplets with radii 16 and 20- μm. In this case, the critical charge is much closer to the estimate ($800\, e$) of Davis [28] than the estimate ($10^4\, e$) of Tinsley and Zhou [29]. However, neither Davis [28] nor Tinsley and Zhou [29] state their value of the radius ratio λ. We find that q_c depends strongly on λ [see Fig. 6(b)], making a direct comparison challenging. Moreover, these earlier estimates did not consider how the hydrodynamic and noncontinuum forces vary at small interfacial distances. While Davis [28] included hydrodynamic forces valid up to $10^{-3}a_2$ (where a_2 is the radius of the larger droplet), he did not account for noncontinuum effects. As a consequence, his results for the collision efficiency depend on an arbitrary cutoff assumed to define a collision [12].

Equation (16) shows how the critical charge q_c depends upon the parameters of the problem. From this equation, we see that $|q_1 q_2| \sim a_2^5$. As mentioned above, Fig. 6(a) confirms this prediction by comparison with numerical simulations which show that $q_c \sim a_2^{2.5}$. This means that the critical charge q_c decreases rapidly as the droplet size decreases. Reference [28], by contrast, used numerical simulations to study which electrical surface-charge density starts to produce droplet collisions. They hypothesized that the critical charge leading to collision behaves as droplet radius squared. Our results instead show that the critical charges scale as $a_2^{5/2}$. This indicates that a charge determined by constant charge density (i.e., scaling proportional to radius squared) is not the factor determining the critical charge. In addition, as discussed above, even though our numerical result seems to match the prediction made by Ref. [28], our analysis explains the mechanism determining the critical charge.

Keeping all parameters the same as in Fig. 4, but with $a_1 = 4\,\mu\text{m}$ and $a_2 = 5\,\mu\text{m}$ and $\text{Kn} = 0.001$, numerical simulations show that a charge of only $30\, e$ is enough to lead to a transition for oppositely charged droplets. Note, however, that spatial diffusion (not considered here) must affect the relative dynamics of such small droplets. In the large charge regime, we verified the validity of our model by comparing to previous experimental results [34] as shown in Fig. 6(c). Our model shows better agreement with experiments compared to the earlier theoretical result of Paluch [30].

The model includes noncontinuum effects due to the breakdown of hydrodynamics at small interfacial distances for both radial and tangential resistance functions. Reference [42] demonstrated that at small Stokes numbers (St), the collision efficiencies match those obtained for a model neglecting inertia (St = 0) from Ref. [12], which did not include noncontinuum corrections to the tangential resistance functions. Therefore, they concluded that while the noncontinuum corrections to tangential resistance functions are negligible at $\mathrm{St} \ll 1$, they might become important for $\mathrm{St} \sim 1$, or when the radius ratio of the droplets deviates significantly from unity [9]. For this reason, we decided to include noncontinuum corrections to the simulations presented in this paper.

Our model has five nondimensional parameters: the Stokes number St (particle inertia), the Coulomb number Cu (charge), the ratio λ of droplet radii, the charge ratio λ_q, and the Knudsen number Kn (effect of mean-free path). We have not yet systematically studied the effect of changing St, λ, and λ_q. Instead we chose $\lambda = 0.8$, $\lambda_q = \pm 1$, and two values of the Stokes number, $\mathrm{St} = 0.48$ and 3.82, for the data in Fig. 4. For computing the Stokes number, and in the simulations we used the values $\nu_{\mathrm{air}} = 1.48 \times 10^{-5}\ \mathrm{m^2/s}$, $\rho_{\mathrm{air}} = 1.22\ \mathrm{kg/m^3}$, $\mu = \nu_{\mathrm{air}}\rho_{\mathrm{air}}$, $\rho_{\mathrm{w}} = 997\ \mathrm{kg/m^3}$, and $g = 9.8\ \mathrm{m/s^2}$. Since the droplet-size distribution in clouds at the onset of collisional growth is narrow [5], it is natural to consider radius ratios close to unity, as we did here. As a next step, it is of interest to study the effect of the parameter λ_q. While the charge distribution of cloud droplets is not known in general, extreme values of λ_q can significantly enhance collision rates [36]. Therefore, it is important to study how the collision efficiency changes as the charge ratio λ_q varies.

Let us briefly comment on the limitations of the model. First, we did not consider van der Waals forces, short-range attractive dipole forces that change the collision dynamics at short interfacial distances s, of the order of the London length λ_L [51]. Rother *et al.* [21] computed the collision rate of droplets settling in still air including van der Waals forces and Maxwell slip (the first-order correction to the noncontinuum effects). They found that van der Waals forces cause a significant increase in the collision rate for droplets smaller than 10 μm in radius, but that the effect is small for larger droplets. This is consistent with the findings of Dhanasekaran *et al.* [12], who stated that van der Waals forces do not matter, compared to noncontinuum effects, for water droplets with radii larger than 10 μm. In order to understand how van der Waals forces affect the collision dynamics of charged droplets, we included the van der Waals force in our simulations, using [51,52]

$$F_{\mathrm{vdW}}^{(\alpha)} = -A_{\mathrm{H}} \begin{cases} \frac{a_1 a_2}{a_1+a_2} \frac{\lambda_L(\lambda_L+7.0768\pi s)}{s^2(\lambda_L+2\pi(1.7692)s)^2} & \text{for} \quad s < 0.25\,\lambda_L/\pi, \\ \frac{a_1 a_2}{a_1+a_2}\left(\frac{4.9\lambda_L}{60\pi s^3} - \frac{6.51\lambda_L^2}{360\pi^2 s^4} + \frac{2.36\lambda_L^3}{1680\pi^3 s^5}\right) & \text{for} \quad s \geqslant 0.25\,\lambda_L/\pi. \end{cases} \tag{18}$$

Here A_{H} is the Hamaker constant, with typical value $A_{\mathrm{H}} = 5 \times 10^{-20}$ J for water droplets in air. Two new nondimensional parameters come with Eq. (18): $\lambda_L/\overline{a}$ quantifies the interfacial separation below which van der Waals forces become important, while $A_{\mathrm{H}}/(\tilde{m}V_0^2)$ quantifies the strength of van der Waals forces with respect to the relative kinetic energy at large separations.

We found that including van der Waals forces in our simulations leads to a small increase of about 15% in the collision efficiency for $\mathrm{Kn} = 0.01$ and droplets of sizes 16 and 20 μm, but does not cause qualitative changes to Figs. 4(a) and 4(d). This is consistent with the findings of Refs. [12,21]. In the limit of small charges and small Kn, by contrast, van der Waals forces may change the collision dynamics qualitatively. We expect that van der Waals forces give rise to a saddle point below the collision sphere, even for neutral droplets. In this case, the stable manifold of this new fixed point may determine the collision efficiency at small values of Kn.

Second, our model uses the Stokes approximation for the hydrodynamic forces and torques. The effects of convective and unsteady fluid inertia were neglected. Klett and Davis [18] explained that convective fluid inertia makes a significant difference to the collision efficiency of droplets with radius ratios close to unity because the droplet dynamics in the Stokes approximation is degenerate when $a_1 = a_2$ (see also Ref. [53]). Magnusson *et al.* [34] considered the leading-order effects of the particle Reynolds number ($\mathrm{Re_p}$) and Strouhal number (Sl) for droplets with $\mathrm{Re_p} \approx 0.1$ and $\mathrm{Sl} \approx 0.1$,

at large droplet separations. Here we do not consider these effects because we do not know how to account for their combined effects at small interfacial distances.

Third, we assumed that the droplets remain spherical before they collide. Yoon *et al.* [20] studied the deformation and coalescence of neutrally buoyant droplets in a straining flow. They used numerical simulations to study how droplet collision dynamics depend on the capillary numbers, Ca, of the droplets, defined as the ratio between the viscous force ($\mu 2a_\alpha |\boldsymbol{V}|$) and the product of surface tension and droplet diameter. Their droplets remain spherical up to contact for capillary numbers smaller than a critical value. In our case, the capillary number is $\sim 10^{-6}$, much smaller than the Yoon *et al.* estimate of the critical capillary number $\sim 10^{-4}$ for 20-μm droplets. While this estimate supports the spherical droplet assumption used in our study, it is not known how the critical capillary number varies with charge, particle inertia, and fluid inertia. An alternative parameter determining droplet deformation is the Weber number $\mathrm{We} = \mathrm{Re_p Ca}$ [54]. When the Weber number is much smaller than unity, as for a 20-μm droplet settling at its terminal velocity ($\mathrm{We} \sim 10^{-6}$), droplet deformation is negligible. At much larger collision speeds the Weber number is larger, and the droplets are expected to deform. This changes not only the electrostatic forces, but also the hydrodynamic forces and their noncontinuum regularizations, effects not considered here.

Fourth, we assumed that the droplets are perfect conductors. The timescale τ_C of charge redistribution on a water droplet depends on the ratio of the permittivity of water ε_w to its electrical conductivity σ, $\tau_\mathrm{C} = \varepsilon_\mathrm{w}/\sigma$ [55]. With the conservative estimate $\sigma \sim 5 \times 10^{-6}\,\mathrm{S\,m^{-1}}$ for pure water, and $\varepsilon_\mathrm{w} \sim 7 \times 10^{-10}\,\mathrm{F\,m^{-1}}$ [56], one finds $\tau_\mathrm{C} \sim 1.4 \times 10^{-4}$ s. This time is much shorter than the shortest timescale of the relative droplet dynamics, $|\tau_{\mathrm{p},1} - \tau_{\mathrm{p},2}|$, for well-separated particles, where $\tau_{\mathrm{p},\alpha}$ are the Stokes times of individual droplets.. For a pair of 16- and 20-μm droplets, one finds $\tau_\mathrm{C}/|\tau_{\mathrm{p},1} - \tau_{\mathrm{p},2}| \sim 0.08$. The small but nonzero charge relaxation may still have a small effect on the electrostatic forces which we neglected. Patra *et al.* [17] included regularization of the attractive electrostatic force due to finite conductivity in their study of collisions between noninertial charged droplets. This regularization only affects dynamics at small interfacial distances. We expect that it will not give qualitative changes to collision efficiencies for the considered range of Kn values, including those relevant in clouds. However, in related but distinct contexts, nonzero charge redistribution time can lead to complex dynamics due to electrohydrodynamic effects [57]. One example is emulsions where droplets are not perfect conductors and their surrounding fluid is not a perfect dielectric. In this case, electrical forces can become coupled to viscous flows leading to charge-driven deformation affecting the collision dynamics [26]. A second example is tip streaming from droplets subject to an external electric field, an effect which is a direct consequence of the finite conductivity of the droplet and is absent for perfectly conducting droplets [27].

Fifth, we considered special initial conditions. We assumed that the droplets are initially so far apart that they settle independently with their respective Stokes settling speeds, and we set their initial angular velocities to zero. As a result, the separatrices shown in Fig. 4 correspond to intersections between the invariant manifolds and the one-parameter family of curves determined by the initial conditions.

Sixth, we considered droplets settling in still air. What is the effect of turbulence on the collision efficiency of charged droplets? Saffman and Turner [6] explained how turbulent strains increase collision rates of cloud droplets, neglecting their interactions. Dhanasekaran *et al.* [12] analyzed how hydrodynamic interactions and their regularization due to the breakdown of hydrodynamics affect the collision dynamics of droplets settling in a steady straining flow. They found much smaller collision rates than Saffman and Turner, and that hydrodynamic interactions lead to an intricate dependence of the collision rate on the straining flow. This behavior is explained by a sequence of bifurcations, both bifurcations of equilibria and grazing bifurcations [11]. It remains an open question as to how electrostatic interactions change this picture. Moreover, the close approach of charged droplets in turbulence was measured in Refs. [47–49], and compared with a theory valid for large droplet separations, similar to the model described by Magnusson *et al.* [34]. In order to quantitatively describe the relative dynamics of nearby droplets, we intend to generalize the model

to arbitrary linear flows. In the presence of a background flow, convective-inertia effects may give rise to inertial lift forces [58].

Finally, we considered droplet charges much smaller than the Rayleigh limit ($\sim 1.3 \times 10^6 e$ for 20-μm droplets) [59]. The Rayleigh limit quantifies the amount of electrical charge a droplet can acquire before the electrical repulsion overcomes the surface tension holding the droplet together, leading to droplet fission [60].

V. CONCLUSIONS

We analyzed the collision dynamics of weakly charged, μm-sized water droplets settling in still air by numerical integration of a model that incorporates particle inertia, hydrodynamic interactions in the Stokes approximation, noncontinuum effects, and electrical forces. We observed two distinct collision regimes. For small charges, the collision dynamics is dominated by short-range hydrodynamic interactions. In this regime it is crucial to take into account how these interactions are regularized below the mean-free path of air. As a consequence, the collision efficiency depends on the Knudsen number Kn in this regime. At large charges, in contrast, the collision efficiency does not depend on Kn because the separatrix between colliding and noncolliding trajectories is the stable manifold of a saddle point far from the collision sphere, consistent with the conclusions drawn in Magnusson *et al.* [34].

The two regimes shown in Fig. 1(b) occur both for droplet pairs with excess charges of the same and of different polarities. This may be surprising at first sight, considering that equal point charges repel each other, while opposite point charges attract. The reason is that induced charges cause the electrostatic force to always be attractive, at small enough separations [35]. Reference [36] describes how induced electrical charges enhance the collision rate between a charged droplet and neutral droplet, where the effect of induced charges is apparent at large separations (where their model applies). For micron-sized droplets of similar sizes, the electrostatic force changes sign at an interfacial distance much smaller than the droplet radius. But since this distance is of the order of the mean-free path, where the hydrodynamic approximation breaks down, the induced charges have a significant effect on the collision efficiency, as we demonstrated in this paper.

We found that the saddle point S1 (Fig. 4) below the collision sphere exists even at small charges. But when the interfacial distance at the saddle point $s^* < \ell$, its stable manifolds depend on the Knudsen number. As a result the collision efficiency depends on Kn, at small charges. The crossover between the two limits occurs when the saddle point moves further away from the collision sphere than the mean-free path. The critical charge where this qualitative change in the collision dynamics occurs is much lower than that stated by Tinsley and Zhou [29]. While our prediction matches that of Davis [28], they did not include noncontinuum effects at small separations, so that their result depends upon the cutoff used to define a collision. We observed that for 20- μm droplets, the transition between the two regimes happens at $\sim 10^3\, e$ for droplets charged with opposite polarities, and at $\sim 10^4\, e$ for droplets charged with the same polarities. These charge magnitudes are comparable to those observed for thunder-cloud droplets [22]. Note, however, that in thunder clouds, electric fields affect the droplet dynamics. Here we did not consider this effect. Zhang *et al.* [24] showed that the attractive force between neutral, conducting droplets due to induced charges caused by external electrical fields increase the collision efficiency and collision rate of droplets settling in under gravity. They found that the collision efficiency exhibits a plateau for when the attractive force is much weaker compared to gravity but increases as the electric field induced force increases (Figs. 7 and 9 in their paper). While we have ignored the effect of external electric fields in this paper, we hypothesize that the theory developed in this paper can be used to estimate the critical nondimensional electric field induced force at which the transition occurs, as well as understand the mechanism underlying this effect.

The conclusions above are based on a model with five nondimensional parameters, and we have only analyzed a small part of the parameter space. Including van der Waals forces give rise to two additional nondimensional parameters [21,51], one quantifying the interfacial separation below

which the van der Waals force is important, and another quantifying its strength. While previous studies [12,21] suggest that including van der Waals force does not give rise to qualitative changes in the dynamics for the parameters typical of cloud droplets with radii larger than 10 μm, we expect that the qualitative dynamics are different when the Knudsen number becomes vanishingly small. The reason is that the attractive van der Waal force gives rise to a saddle point below, which determines the relative dynamics for vanishingly small Knudsen numbers.

Finally, we assumed here that the droplets settle in quiescent air. We did not consider the effects of turbulent flow. Turbulence can substantially increase the rate at which droplets collide [6,12] because turbulent strains bring similar-sized droplets together. Atten [25] investigated the collision rate of conducting droplets suspended in a flowing, insulating liquid in the presence of an external electric field in order to understand the mechanisms underlying a high-efficiency electrocoalescer. He proposed that the high efficiency could be attributed to a two-stage process: a first stage where droplets approach each other driven by the shear and a second stage where droplets are brought together due to shear coalesce rapidly because the electric field decreases the characteristic coalescence time by several orders of magnitude. However, the combined effect of shear and electrical forces has not been quantitatively studied so far. More generally, turbulence increases spatial clustering of droplets, as measured by the pair-correlation function (see Ref. [15] for a review). Lu *et al.* [47–49] measured how electrical charges change the pair-correlation function, and developed models to explain the observed effects, at separations much larger than the droplet radii where hydrodynamic interactions can be neglected. It would be of interest to include in the model the mechanisms described here, in order to determine how charges affect the pair-correlation function at smaller separations. Similarly, the relative-velocity statistics of charged droplets in turbulence was investigated in Ref. [61], neglecting hydrodynamic interactions. Our results indicate that these interactions (and their regularization by noncontinuum effects) cannot be neglected at small separations. In summary, the phase-space picture presented above shows that fairly small charges can have a significant effect on the relative droplet dynamics. How this affects the pair-correlation function, relative-velocity statistics, and collision efficiencies in turbulence remains an open question.

ACKNOWLEDGMENTS

The research of A.D. and B.M. was supported by grants from Vetenskapsrådet (Grants No. 2017-3865 and No. 2021-4452) and from the Knut and Alice Wallenberg Foundation (Grant No. 2014.0048). The research of G.P.B. was supported by the National Science Foundation under Grants No. CBET-1605195 and No. AGS-2133229. B.M. acknowledges a Mary Shepard B. Upson Visiting Professorship with the Sibley School of Mechanical and Aerospace Engineering at Cornell.

APPENDIX: FUNCTIONS $f_{\rm fit}^{\parallel}$, $\widetilde{Q}$, AND $\widetilde{W}$ USED TO DEFINE THE NONCONTINUUM RESISTANCE FUNCTIONS

Here we list the functions $f_{\rm fit}^{\parallel}$, $\widetilde{Q}$, and $\widetilde{W}$ which are required to define the noncontinuum resistance functions in Sec. II, reproduced from Ref. [9]. These are given by

$$f_{\rm fit}^{\parallel} = \begin{cases} \frac{\pi}{6}\left(\ln t - \frac{1}{t} - \frac{1}{t^2} - \frac{2}{t^3}\right) + 1.5475\delta_0^2 + 0.7896\delta_0 + 0.4094, & \delta_0 < 0.35 \\ 0.00006\frac{1}{\delta_0^3} - 0.00172\frac{1}{\delta_0^2} + 0.0169\frac{1}{\delta_0} + 0.1769\ln\frac{1}{\delta_0} + 0.3744, & 0.35 < \delta_0 < 0.9 \\ 0.0005\delta_0^4 - 0.00835\delta_0^3 + 0.05605\delta_0^2 - 0.2196\delta_0 + 0.5661 & \\ \quad -0.0055\frac{1}{\delta_0} - 0.01965\frac{1}{\delta_0^2} + 0.0231\frac{1}{\delta_0^3}, & 0.9 < \delta_0 < 4.4 \\ \frac{1}{18k_1^2}\left[(6k_1+\delta_0)\ln\left(1+\frac{6k_1}{\delta_0}\right) - 6k_1\right], & \delta_0 > 4.4 \end{cases} \tag{A1}$$

where $t = \ln(1/\delta_0) + 0.8$, $\delta_0 = (R/\overline{a} - 2)/\mathrm{Kn}$, and $k_1 = 1.016$,

$$\widetilde{Q} = \frac{b_1 + b_2 \ln\left(\frac{1}{\delta_0} + b_3\right)}{1 + b_4\delta_0}, \tag{A2}$$

where $b_1 = -0.1580$, $b_2 = -1/5$, $b_3 = 0.65632$, and $b_4 = 0.16330$, and

$$\widetilde{W} = \frac{b_5 + b_6 \ln\left(\frac{1}{\delta_0} + b_7\right)}{1 + b_8\delta_0}, \tag{A3}$$

where $b_5 = -1.6448$, $b_6 = -\sqrt{\pi}$, $b_7 = 0.59098$, and $b_8 = 0.19167$.

In the limit of $\mathrm{Kn} \to 0$, these simplify to $f_{\mathrm{fit}}^{\parallel} \sim \frac{1}{3k_1} + \frac{1}{\delta_0}$ and $\widetilde{Q} = \widetilde{W} = 0$.

[1] H. R. Pruppacher and J. D. Klett, *Microphysics of Clouds and Precipitation*, 2nd ed. (Kluwer Academic, Dordrecht, The Netherlands, 1997), p. 954.

[2] R. A. Shaw, Particle-turbulence interactions in atmospheric clouds, Annu. Rev. Fluid Mech. **35**, 183 (2003).

[3] B. J. Devenish, P. Bartello, J. L. Brenguier, L. R. Collins, W. W. Grabowski, R. H. Ijzermans, S. P. Malinowski, M. W. Reeks, J. C. Vassilicos, L. P. Wang, and Z. Warhaft, Droplet growth in warm turbulent clouds, Q. J. R. Meteorol. Soc. **138**, 1401 (2012).

[4] E. X. Berry and R. L. Reinhardt, An analysis of cloud drop growth by collection: Part I. Double distributions, J. Atmos. Sci. **31**, 1814 (1974).

[5] W. W. Grabowski and L.-P. Wang, Growth of cloud droplets in a turbulent environment, Annu. Rev. Fluid Mech. **45**, 293 (2013).

[6] P. G. Saffman and J. S. Turner, On the collision of drops in turbulent clouds, J. Fluid Mech. **1**, 16 (1956).

[7] A. B. Kostinski and R. A. Shaw, Fluctuations and luck in droplet growth by coalescence, Bull. Am. Meteorol. Soc. **86**, 235 (2005).

[8] S. Kim and S. J. Karrila, *Microhydrodynamics: Principles and Selected Applications* (Butterworth-Heinemann, Boston, 1991).

[9] M. Li Sing How, D. L. Koch, and L. R. Collins, Non-continuum tangential lubrication gas flow between two spheres, J. Fluid Mech. **920**, A2 (2021).

[10] R. R. Sundararajakumar and D. L. Koch, Non-continuum lubrication flows between particles colliding in a gas, J. Fluid Mech. **313**, 283 (1996).

[11] A. Dubey, K. Gustavsson, G. P. Bewley, and B. Mehlig, Bifurcations in droplet collisions, Phys. Rev. Fluids **7**, 064401 (2022).

[12] J. Dhanasekaran, A. Roy, and D. L. Koch, Collision rate of bidisperse spheres settling in a compressional non-continuum gas flow, J. Fluid Mech. **910**, A10 (2021).

[13] S. Sundaram and L. R. Collins, Collision statistics in an isotropic particle-laden turbulent suspension, J. Fluid Mech. **335**, 75 (1997).

[14] G. Falkovich, I. Fouxon, and M. G. Stepanov, Acceleration of rain initiation by cloud turbulence, Nature (London) **419**, 151 (2002).

[15] K. Gustavsson and B. Mehlig, Statistical models for spatial patterns of heavy particles in turbulence, Adv. Phys. **65**, 1 (2016).

[16] K. Sambath, V. Garg, S. S. Thete, H. J. Subramani, and O. A. Basaran, Inertial impedance of coalescence during collision of liquid drops, J. Fluid Mech. **876**, 449 (2019).

[17] P. Patra, D. L. Koch, and A. Roy, Collision efficiency of like-charged spheres settling in a quiescent environment, J. Fluid Mech. **968**, A22 (2023).

[18] J. D. Klett and M. Davis, Theoretical collision efficiencies of cloud droplets at small Reynolds numbers, J. Atmos. Sci. **30**, 107 (1973).

[19] F. Candelier, Relative motion of two identical bubbles, rising in a fluid at rest, at small Reynolds numbers, C. R. Mec. **335**, 732 (2007).
[20] Y. Yoon, F. Baldessari, H. D. Ceniceros, and L. G. Leal, Coalescence of two equal-sized deformable drops in an axisymmetric flow, Phys. Fluids **19**, 102102 (2007).
[21] M. Rother, J. Stark, and R. Davis, Gravitational collision efficiencies of small viscous drops at finite Stokes numbers and low Reynolds numbers, Int. J. Multiphase Flow **146**, 103876 (2022).
[22] T. Takahashi, Measurement of electric charge of cloud droplets, drizzle, and raindrops, Rev. Geophys. **11**, 903 (1973).
[23] R. G. Harrison, K. A. Nicoll, and M. H. P. Ambaum, On the microphysical effects of observed cloud edge charging, Q. J. R. Meteorol. Soc. **141**, 2690 (2015).
[24] X. Zhang, O. A. Basaran, and R. M. Wham, Theoretical prediction of electric field-enhanced coalescence of spherical drops, AIChE J. **41**, 1629 (1995).
[25] P. Atten, Electrocoalescence of water droplets in an insulating liquid, J. Electrost. **30**, 259 (1993).
[26] J. C. Baygents, N. Rivette, and H. A. Stone, Electrohydrodynamic deformation and interaction of drop pairs, J. Fluid Mech. **368**, 359 (1998).
[27] R. T. Collins, K. Sambath, M. T. Harris, and O. A. Basaran, Universal scaling laws for the disintegration of electrified drops, Proc. Natl. Acad. Sci. USA **110**, 4905 (2013).
[28] M. H. Davis, The effect of electric charges and fields on the collision of very small cloud drops, in *Proceedings of the International Conference on Cloud Physics, Tokyo and Sapporo* (Organizing Committee, Tokyo, 1965).
[29] B. Tinsley and L. Zhou, Comments on "Effect of electric charge on collisions between cloud droplets", J. Appl. Meteorol. Climatol. **53**, 1317 (2014).
[30] I. Paluch, Theoretical collision efficiencies of charged cloud droplets, J. Geophys. Res. (1896-1977) **75**, 1633 (1970).
[31] R. J. Schlamp, S. N. Grover, H. R. Pruppacher, and A. E. Hamielec, Numerical investigation of the effect of electric charges and vertical external electric fields on the collision efficiency of cloud drops, J. Atmos. Sci. **33**, 1747 (1976).
[32] R. J. Schlamp, S. N. Grover, H. R. Pruppacher, and A. E. Hamielec, A numerical investigation of the effect of electric charges and vertical external electric fields an the collision efficiency of cloud drops: Part II, J. Atmos. Sci. **36**, 339 (1979).
[33] C. E. Abbott, Experimental cloud droplet collection efficiencies, J. Geophys. Res. **79**, 3098 (1974).
[34] G. Magnusson, A. Dubey, R. Kearney, G. P. Bewley, and B. Mehlig, Collisions of micron-sized charged water droplets in still air, Phys. Rev. Fluids **7**, 043601 (2022).
[35] J. Lekner, Electrostatics of two charged conducting spheres, Proc. R. Soc. A **468**, 2829 (2012).
[36] A. Khain, V. Arkhipov, M. Pinsky, Y. Feldman, and Y. Ryabov, Rain enhancement and fog elimination by seeding with charged droplets. Part I: Theory and numerical simulations, J. Appl. Meteorol. **43**, 1513 (2004).
[37] N. H. Fletcher, Effect of electric charge on collisions between cloud droplets, J. Appl. Meteorol. Climatol. **52**, 517 (2013).
[38] D. J. Jeffrey and Y. Onishi, Calculation of the resistance and mobility functions for two unequal rigid spheres in low-Reynolds-number flow, J. Fluid Mech. **139**, 261 (1984).
[39] D. J. Jeffrey, Conduction through a random suspension of spheres, Proc. R. Soc. London, Ser. A **335**, 355 (1973).
[40] A. K. Townsend, Generating, from scratch, the near-field asymptotic forms of scalar resistance functions for two unequal rigid spheres in low-Reynolds-number flow, arXiv:1802.08226.
[41] H. Wang, A. Z. Zinchenko, and R. H. Davis, The collision rate of small drops in linear flow fields, J. Fluid Mech. **265**, 161 (1994).
[42] M. Li Sing How, Numerical simulation of near-contact motion and coalescence of inertial droplets in turbulence, Ph.D. thesis, Cornell, 2021.
[43] P. L. Bhatnagar, E. P. Gross, and M. Krook, A model for collision processes in gases. I. Small amplitude processes in charged and neutral one-component systems, Phys. Rev. **94**, 511 (1954).
[44] J. D. Jackson, *Classical Electrodynamics,* 2nd ed. (Wiley, New York, 1975).

[45] W. R. Smythe, *Static and Dynamic Electricity*, 3rd ed. (McGraw-Hill, New York, 1967), includes bibliographies and index.
[46] G. M. Hidy and J. R. Brock, Some remarks about the coagulation of aerosol particles by Brownian motion, J. Colloid Sci. **20**, 477 (1965).
[47] J. Lu, H. Nordsiek, E. W. Saw, and R. A. Shaw, Clustering of charged inertial particles in turbulence, Phys. Rev. Lett. **104**, 184505 (2010).
[48] J. Lu, H. Nordsiek, and R. A. Shaw, Clustering of settling charged particles in turbulence: theory and experiments, New J. Phys. **12**, 123030 (2010).
[49] J. Lu and R. A. Shaw, Charged particle dynamics in turbulence: Theory and direct numerical simulations, Phys. Fluids **27**, 065111 (2015).
[50] S. Wiggins, *Chaotic Transport in Dynamical Systems*, Interdisciplinary Applied Mathematics (Springer, New York, 2013).
[51] X. Zhang and R. H. Davis, The rate of collisions due to Brownian or gravitational motion of small drops, J. Fluid Mech. **230**, 479 (1991).
[52] N. F. H. Ho and W. I. Higuchi, Preferential aggregation and coalescence in heterodispersed systems, J. Pharm. Sci. **57**, 436 (1968).
[53] F. Candelier and B. Mehlig, Settling of an asymmetric dumbbell in a quiescent fluid, J. Fluid Mech. **802**, 174 (2016).
[54] J. Qian and C. K. Law, Regimes of coalescence and separation in droplet collision, J. Fluid Mech. **331**, 59 (1997).
[55] H. A. Haus and J. R. Melcher, *Electromagnetic Fields and Energy* (Prentice-Hall, Englewood Cliffs, NJ, 1989).
[56] J. Rumble, *CRC Handbook of Chemistry and Physics*, 103rd ed. (Taylor & Francis, London, 2022).
[57] J. Melcher and G. Taylor, Electrohydrodynamics: a review of the role of interfacial shear stresses, Annu. Rev. Fluid Mech. **1**, 111 (1969).
[58] F. Candelier, B. Mehlig, and J. Magnaudet, Time-dependent lift and drag on a rigid body in a viscous steady linear flow, J. Fluid Mech. **864**, 554 (2019).
[59] L. Rayleigh, XX. On the equilibrium of liquid conducting masses charged with electricity, London Edinburgh Philos. Mag. & J. Sci. **14**, 184 (1882).
[60] D. C. Taflin, T. L. Ward, and E. J. Davis, Electrified droplet fission and the rayleigh limit, Langmuir **5**, 376 (1989).
[61] V. M. Alipchenkov, L. I. Zaichik, and O. F. Petrov, Clustering of charged particles in isotropic turbulence, High Temp. **42**, 919 (2004).